

## MULTI-WAVELENGTH OBSERVATIONS OF THE DISSOCIATIVE MERGER IN THE GALAXY CLUSTER CIZA J0107.7+5408

S. W. RANDALL<sup>1</sup>, T. E. CLARKE<sup>2</sup>, R. J. VAN WEEREN<sup>1</sup>, H. T. INTEMA<sup>3</sup>, W. A. DAWSON<sup>4</sup>, T. MROCKZKOWSKI<sup>5</sup>, E. L. BLANTON<sup>6</sup>, E. BULBUL<sup>7</sup>, S. GIACINTUCCI<sup>8</sup>

*Accepted version of April 14, 2016*

### ABSTRACT

We present results based on X-ray, optical, and radio observations of the massive galaxy cluster CIZA J0107.7+5408. We find that this system is a post core passage, dissociative, binary merger, with the optical galaxy density peaks of each subcluster leading their associated X-ray emission peaks. This separation occurs because the diffuse gas experiences ram pressure forces while the effectively collisionless galaxies (and presumably their associated dark matter halos) do not. This system contains double peaked diffuse radio emission, possibly a double radio relic with the relics lying along the merger axis and also leading the X-ray cores. We find evidence for a temperature peak associated with the SW relic, likely created by the same merger shock that is powering the relic radio emission in this region. Thus, this system is a relatively rare clean example of a dissociative binary merger, which can in principle be used to place constraints on the self-interaction cross-section of dark matter. Low frequency radio observations reveal ultra-steep spectrum diffuse radio emission that is not correlated with the X-ray, optical, or high frequency radio emission. We suggest that these sources are radio phoenixes, which are preexisting non-thermal particle populations that have been re-energized through adiabatic compression by the same merger shocks that power the radio relics. Finally, we place upper limits on inverse Compton emission from the SW radio relic.

*Subject headings:* dark matter — galaxies: clusters: general — galaxies: clusters: individual (CIZA J0107.7+5408) — galaxies: clusters: intracluster medium — X-rays: galaxies: clusters

### 1. INTRODUCTION

According to the standard model of hierarchical structure formation, galaxy clusters largely grow through cluster mergers. Major mergers are the most energetic events in the Universe since the Big Bang, and can release  $\gtrsim 10^{64}$  erg in gravitational binding energy. Such mergers significantly disturb the intracluster medium (ICM) of galaxy clusters, and are useful for the study of ICM plasma physics, cluster scaling relations, non-thermal particle populations, the growth of large scale structure, and the physics of dark matter.

Dissociative mergers occur when the ICM of a merging subcluster experiences sufficient ram pressure forces to displace it from the gravitational potential minimum of its dark matter halo. Such offsets are observed as separations between the X-ray surface brightness peaks and/or the optical galaxy density and gravitational lens-

ing mass peaks, where the effectively collisionless galaxies are expected to trace their dark matter halos. Such systems, e.g., the well-known Bullet Cluster (Markevitch et al. 2002), have been used to demonstrate the existence of dark matter, and to place limits on the self-interaction cross-section of dark matter, since self-interacting dark matter would experience ram-pressure-like forces during a merger, potentially leading to an offset between the optical galaxies and the dark matter peak (e.g., Markevitch et al. 2004; Clowe et al. 2006; Bradač et al. 2006; Clowe et al. 2007; Randall et al. 2008b; Dawson et al. 2012; Harvey et al. 2015).

Merging or otherwise dynamically disturbed systems often host diffuse radio sources. These sources can be broadly divided into at least three categories: radio relics, radio halos, and radio phoenixes (for a review see Feretti et al. 2012). Relics are typically found in the outskirts of clusters, and often have large sizes ( $\gtrsim 1$  Mpc) and polarized emission. In contrast, halos are centered on cluster cores, and are typically not strongly polarized. The location and morphology of radio phoenixes varies widely, although they are typically smaller than relics and halos. Relics, halos, and phoenixes are thought to be powered by cluster mergers, through direct shock acceleration, merger induced turbulence, and adiabatic compression by shocks, respectively (Blandford & Eichler 1987; Brunetti et al. 2001; Enßlin & Gopal-Krishna 2001; Brunetti & Jones 2015). Observationally, ultra-steep spectrum (USS) diffuse radio sources with radio spectral indices  $\alpha \lesssim -1.5^9$  (such as those described by Slee et al. 2001) represent a particular subset of sources.

<sup>1</sup> Harvard-Smithsonian Center for Astrophysics, 60 Garden St., Cambridge, MA 02138, USA; [srandall@cfa.harvard.edu](mailto:srandall@cfa.harvard.edu)

<sup>2</sup> Naval Research Laboratory, 4555 Overlook Avenue SW, Code 7213, Washington, DC 20375, USA

<sup>3</sup> National Radio Astronomy Observatory, 1003 Lopezville Road, Socorro, NM 87801-0387, USA

<sup>4</sup> Lawrence Livermore National Lab, 7000 East Avenue, Livermore, CA 94550, USA

<sup>5</sup> U.S. Naval Research Laboratory, 4555 Overlook Avenue SW, Washington, DC 20375, USA

<sup>6</sup> Astronomy Department and Institute for Astrophysical Research, Boston University, 725 Commonwealth Avenue, Boston, MA 02215, USA

<sup>7</sup> Kavli Institute for Astrophysics & Space Research, Massachusetts Institute of Technology, 77 Massachusetts Ave, Cambridge, MA 02139, USA

<sup>8</sup> Department of Astronomy, University of Maryland, College Park, MD 20742-2421, USA

<sup>9</sup> Where the radio flux  $F_\nu \propto \nu^\alpha$ .

It is currently unknown whether these sources are typically weaker “classical” radio relics associated with more minor mergers, radio phoenixes, “AGN relics” (associations of old radio plasma left over from a previous AGN outburst, Murgia et al. 2012), or some mix of these three. New low-frequency radio survey instruments such as LOFAR (van Haarlem et al. 2013) are expected to find large numbers of such diffuse USS sources (Röttgering et al. 2011).

Here we present results from *Chandra*, X-ray; VLA, WSRT, and GMRT radio; and INT optical observations of the galaxy cluster CIZA J0107.7+5408 (hereafter CIZA 0107), at a redshift of  $z = 0.1066$  (Ebeling et al. 2002), which contains both high and low frequency diffuse radio emission. The primary aims of this paper are to characterize the dynamical state of CIZA 0107; search for merger signatures (such as disturbed morphology and shock fronts); compare X-ray, optical, and radio observations to investigate the nature of the diffuse radio emission; and to evaluate the potential for this system to probe ICM and dark matter physics. When corrected to the reference frame defined by the CMB<sup>10</sup>, the redshift corresponds to a luminosity distance of  $D_L = 470$  Mpc and a scale of  $1.86 \text{ kpc arcsec}^{-1}$  for a cosmology with  $\Omega_0 = 0.3$ ,  $\Omega_\Lambda = 0.7$ , and  $H_0 = 73 \text{ km s}^{-1} \text{ Mpc}^{-1}$ . All uncertainty ranges are 68% confidence intervals (i.e.,  $1\sigma$ ), unless otherwise stated.

## 2. DATA ANALYSIS

### 2.1. *Chandra* X-ray Observations

CIZA 0107 was observed by *Chandra* for 23 ks on 2013 June 26 (ObsID 15152). The aimpoint was on the front-side illuminated ACIS-I CCD. All data were reprocessed from the level 1 event files using CIAO and CALDB 4.6.7. CTI and time-dependent gain corrections were applied. LC\_CLEAN was used to check for periods of background flares<sup>11</sup>. The mean event rate was calculated from a source free region using time bins within  $3\sigma$  of the overall mean, and bins outside a factor of 1.2 of this mean were discarded. There were no periods of strong background flares, such that the cleaned exposure time was 23 ks. To model the background we used the CALDB<sup>12</sup> blank sky background files appropriate for this observation, normalized to match the 10–12 keV count rate in our observations to account for variations in the particle background. Point sources were detected using the CIAO tool WAVDETECT, and source regions were checked by eye and subsequently excluded from the analysis. The background subtracted, exposure corrected *Chandra* image of the full ACIS-I field of view (FOV) is shown in Figure 1.

Unless otherwise specified, all spectra were fitted in the 0.7–8.0 keV band using XSPEC, with an absorbed APEC model. Spectra were grouped with a minimum of 40 counts per energy bin. Grevesse & Sauval (1998) abundance ratios and ATOMDB 2.0.2 (Foster et al. 2012) were used throughout.

<sup>10</sup> The NASA/IPAC Extragalactic Database (NED) is operated by the Jet Propulsion Laboratory, California Institute of Technology, under contract with the National Aeronautics and Space Administration.

<sup>11</sup> <http://asc.harvard.edu/contrib/maxim/acisbg/>

<sup>12</sup> <http://cxc.harvard.edu/caldb/>

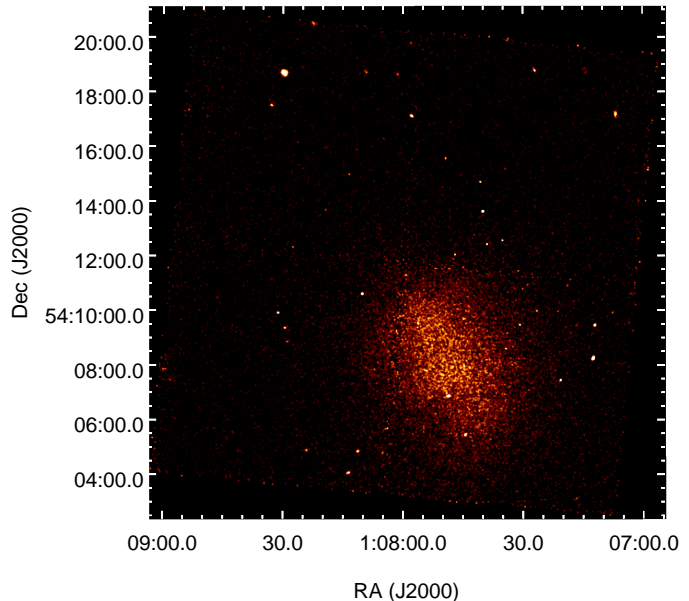


**Figure 1.** *Chandra* 0.3–8.0 keV X-ray image of the full ACIS-I FOV, background subtracted and exposure corrected, and smoothed with a  $3''$  radius Gaussian.

### 2.2. WSRT Radio Observations

We use the 1.4 GHz WSRT radio observations presented in van Weeren et al. (2011a). The 1.4 GHz image of the cluster has a noise levels of  $29 \mu\text{Jy beam}^{-1}$  and a resolution of  $21'' \times 17''$ . In addition, we make use of a lower-resolution image with a resolution of  $60''$  and with emission from compact sources subtracted to better bring out the diffuse emission. For radio imaging, we used a Briggs weighting scheme with a robust parameter of 0.5 for the full image and natural weighting with a UV-taper for the source subtracted image. For more details about these observations and the data reduction the reader is referred to van Weeren et al. (2011a).

### 2.3. GMRT Radio Observations

On 2009 November 23, CIZA 0107 was observed with the GMRT (Swarup 1991) simultaneously at 240 and 610 MHz within the scope of a larger project to study newly discovered radio relics (project code 17\_049; PI van Weeren). The total time on-source was about 200 minutes. For reducing the data, we used the SPAM package and a standard data reduction recipe as described in Intema et al. (2009); Intema (2014). We used the primary calibrator 3C48 for deriving all instrumental calibrations, adopting the Scaife & Heald (2012) flux scale. The effective bandwidth used for imaging was 6.5 and 32.8 MHz at 240 and 610 MHz, respectively. The final images were made at resolutions of  $13.3'' \times 10.4''$  and  $5.7'' \times 4.1''$ , respectively. The achieved background RMS noises as measured in the center of the beam were  $0.57$  and  $0.054 \text{ mJy beam}^{-1}$ , respectively. We complemented these targeted observations with a 150 MHz image made from archival TGSS<sup>13</sup> survey data (project code 18\_031, pointing R04D65), reprocessed by us in exactly the same way as described above. Using 16 MHz of bandwidth, and using 3C147 as our primary calibrator, we obtained an

<sup>13</sup> <http://tgss.ncra.tifr.res.in/>

image with resolution of  $29.5'' \times 21.9''$ , and a local background RMS noise near the target of  $13 \text{ mJy beam}^{-1}$ . All GMRT images were created using Briggs weighting with a robust parameter of -1 to achieve a more stable PSF.

#### 2.4. VLA Radio Observations

We use the 73.8 MHz Very Large Array Low-frequency Sky Survey redux (VLSSr, Lane et al. 2014) to measure the low frequency emission in CIZA 0107. We used the standard VLSSr image, which has a spatial resolution of  $75''$  and a measured noise level of  $\sigma_{\text{rms}} = 78 \text{ mJy beam}^{-1}$  in the field around CIZA 0107. We refer the reader to Lane et al. (2014) for details of the image calibration and processing. All flux measurements include a “CLEAN bias” of  $0.66\sigma_{\text{rms}} \text{ beam}^{-1}$  for all regions with fluxes above  $3\sigma_{\text{rms}}$ , following the estimates of Lane et al. (2014).

#### 2.5. Optical Observations

Optical images of CIZA 0107 were taken with the Wide Field Camera (WFC) on the 2.5 m Isaac Newton Telescope (INT) in the  $V$ ,  $R$ , and  $I$  bands. For more details on the data reduction see van Weeren et al. (2011c). We compute galaxy iso-density contours by counting the number of galaxies per unit area on the sky. For this we first created a catalog of objects with SEXTRACTOR (Bertin & Arnouts 1996). We excluded all unresolved objects from the catalog to avoid the numerous foreground stars in the field. To select cluster members we only counted objects with  $V - R$  and  $R - I$  colors within 0.5 magnitude from the average cD colors ( $V - R = 1.0$ ,  $R - I = 0.75$ ). In addition, we required these objects to be fainter than the cDs but brighter than magnitude 22 to reduce contamination from more distant galaxies. This selection gave 220 cluster member galaxies in the region spanned by the galaxy density contours shown in Figure 10.

### 3. THE STRUCTURE OF THE ICM

#### 3.1. Global ICM Properties

We measured the global properties of the ICM by fitting the X-ray spectrum extracted from within a 645 kpc radius with an absorbed APEC model. As a CIZA cluster (Clusters in the Zone of Avoidance, Ebeling et al. 2002; Kocevski et al. 2007), CIZA 0107 is at a relatively low Galactic latitude of  $b \approx -8.6583^\circ$ . Due to the relatively high absorption close to the Galactic plane, we allowed  $N_{\text{H}}$  to vary as a free parameter. This provided an acceptable fit, with  $N_{\text{H}} = 3.5^{+0.1}_{-0.1} \times 10^{21} \text{ cm}^{-2}$ ,  $kT = 7.8^{+0.4}_{-0.3} \text{ keV}$ , and  $Z = 0.31^{+0.05}_{-0.05} Z_{\odot}$ , and with a  $\chi^2$  per degree of freedom of  $\chi^2_{\nu} = 390/378 = 1.03$ . This fitted value for  $N_{\text{H}}$  is significantly larger than the weighted average value from the Leiden/Argentine/Bonn (LAB) survey (Kalberla et al. 2005) of  $N_{\text{H}} = 2.3 \times 10^{21} \text{ cm}^{-2}$ . We find that fixing  $N_{\text{H}}$  at this value gives a much worse fit, with  $kT = 11.9^{+0.6}_{-0.6} \text{ keV}$  and  $\chi^2_{\nu} = 493/379 = 1.30$ . We note that there is some systematic uncertainty at low energies associated with modeling the contamination build-up on the ACIS detector, which will in principle affect our absorption and temperature measurements, however this effect is relatively small,  $\lesssim 10\%$ <sup>14</sup>. We conclude

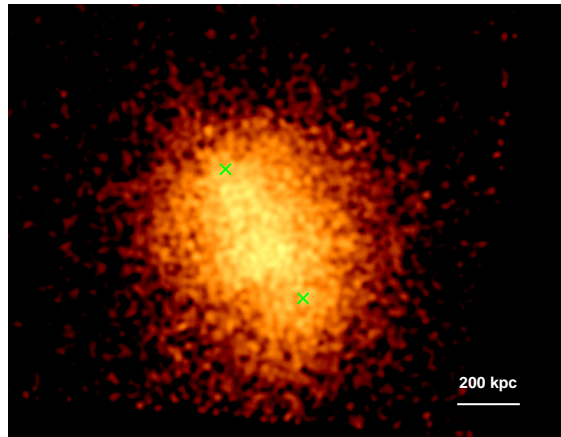


**Figure 2.** *Chandra* 0.3–8.0 keV X-ray image, background subtracted and exposure corrected, and smoothed with a  $10''$  radius Gaussian. Point sources have been removed (see text). The positions of the two BCGs are marked with green crosses. The ICM is elongated from NE to SW, and the two BCGs are offset from the X-ray peak along the same axis.

that  $N_{\text{H}}$  can vary significantly (by at least 50% or so) on angular scales smaller than what is resolved in the LAB survey, (which has a resolution of about  $0.6^\circ$ , larger than the *Chandra* ACIS-I FOV of  $0.27^\circ$  and much larger than *Chandra*’s resolution of  $\sim 0.5''$ ), consistent with results from some more recent, higher angular resolution H I survey maps (e.g., Peek et al. 2011).

We estimated  $r_{500}$ , the radius within which the mean density is equal to 500 times the critical density at the cluster redshift, and  $M_{500}$ , the total mass within  $r_{500}$ , using the  $M_{500} - T_X$  scaling relation of Vikhlinin et al. (2009). The radius was iteratively determined by estimating  $r_{500}$ , measuring the temperature by fitting a spectrum extracted with  $r < 0.15r_{500}$  excluded, determining  $M_{500}$  (and  $r_{500}$ ) from the  $M_{500} - T_X$  relation, and repeating until the values converged. We find  $T_{500} = 7.8^{+0.5}_{-0.5} \text{ keV}$ ,  $M_{500} = 7.8^{+0.8}_{-0.7} \times 10^{14} M_{\odot}$ , and  $r_{500} = 1.35^{+0.05}_{-0.04} \text{ Mpc}$ . We note that these uncertainty ranges only include statistical uncertainties. Systematic uncertainties will likely increase the total uncertainty. Furthermore, cluster mergers can temporarily boost the global temperature, leading to biased temperature measurements and inferred masses (Ricker & Sarazin 2001; Randall et al. 2002). Our derived value for  $M_{500}$  is consistent with the value derived from *Planck* Sunyaev-Zel’dovich observations of  $M_{500,\text{SZ}} = 5.8^{+0.3}_{-0.3} \times 10^{14} M_{\odot}$  within  $3\sigma$  (*Planck* ID PSZ2 G125.37-08.67; *Planck* Collaboration et al. 2014).

#### 3.2. The X-ray Image

The smoothed *Chandra* image of CIZA 0107 is shown in Figure 2. Point sources have been excised, and the resulting gaps filled in by sampling from Poisson distributions matched to local annular background regions. The ICM shows a clear elongation from NE to SW, and no very bright peaks to suggest the presence of a cool core, indicating a dynamically unrelaxed merging system. The central bright X-ray emission is non-circular, and also elongated from NE to SW. A close up view of this “central bar” is shown in Figure 3. The morphology is suggestive of two distinct peaks, with a possible faint extension to the SW.

<sup>14</sup> <http://cxc.harvard.edu/ciao/why/acisqecontam.html>

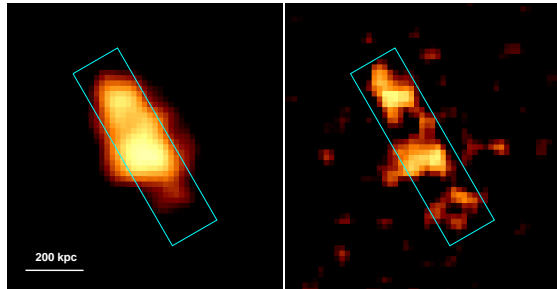


**Figure 3.** Left: *Chandra* image of the core, binned to  $10''$  pixels and smoothed with a  $30''$  radius Gaussian, with the color-map and scale chosen to highlight the bright central bar. Right: Unsharp-masked image of the same field. The light blue rectangular region shows the area used to extract the surface brightness profile shown in Figure 4. There are two prominent peaks, which we identify as the two merging subcluster cores, and possibly a fainter peak to the SW, which may be an enhancement due to a merger bow shock.

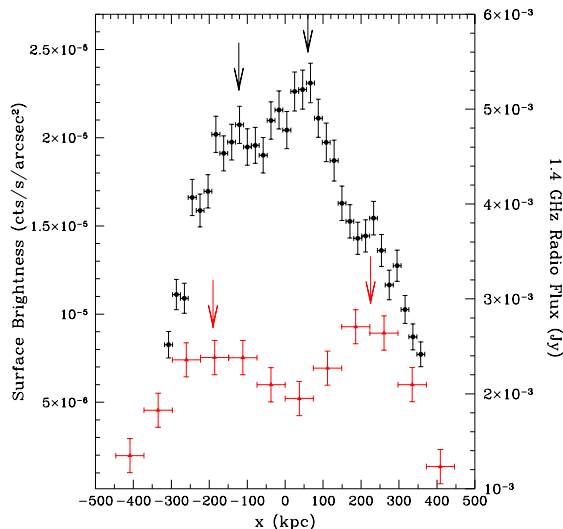


**Figure 4.** Black circles show the 0.3–8 keV X-ray surface brightness profile across the box region shown in Figure 3 (from an unsmoothed image), while red triangles show the 1.4 GHz radio flux across the box shown in Figure 8, from NE to SW.  $x = 0$  corresponds to the center used for the radial profile regions shown in Figure 6. The instrumental resolution is significantly smaller than the size of the individual regions in each case. The black and red arrows indicate the locations of the X-ray and radio peaks, respectively. The two radio peaks are farther out than the two X-ray peaks. There is some evidence for a weak excess in X-ray surface brightness at the location of the SW radio peak, possibly due to ICM compression by a merger bow shock.

To better show subtle structure in the central bar, we created the unsharp-masked image shown in Figure 3. This image was derived by separately smoothing the X-ray image with  $10''$  and  $30''$  radius Gaussians and taking the difference of the results (see Fabian et al. 2006). The two bright peaks are clearly visible, as is a third peak to the SW. We extracted the surface brightness profile across the box region in Figure 3, from NE to SW. The result is shown in Figure 4. The bright central peak is visible at  $\sim 50$  kpc, and the fainter NE peak at  $\sim -125$  kpc. Given the errors, the NE peak may also be consistent with a flattened tail. There is a hint of the faint SW peak between 200–300 kpc, although this feature is not statistically significant.

### 3.3. Thermal Structure

To map the thermal structure of the ICM, we generated smoothed spectral maps using the method described in Randall et al. (2008a). Spectra were extracted from circular regions, centered on each temperature map pixel and containing  $\sim 2000$  source counts in the 0.7–8.0 keV band, and fitted with an absorbed APEC model. Galactic absorption was fixed at the global value derived in Section 3.1. Pixel values were derived from the fitted model parameters. For comparison, we also constructed a temperature map using the contour binning method developed by Sanders (2006), where extraction regions are defined based on surface brightness contours, using a signal-to-noise (S/N) ratio of 44 per region.

The *Chandra* temperature, pseudo-entropy, and pseudo-pressure maps are shown in Figure 5. Both the smoothed and the contour binned temperature maps show a high temperature region to the SW, beyond the X-ray surface brightness peaks, and in the region of the SW optical galaxy density peak and the bright SW radio relic (Section 4). This region appears as a pressure peak in the pseudo-pressure map. The pseudo-entropy map shows a central low entropy region that is extended from NE to SW, consistent with the presence of two partially disrupted, merging cluster cores. Thus, the spectral maps support a roughly head-on merger scenario with a NE–SW merger axis, with two subcluster cores and the presence of high-temperature, shock-heated gas to the SW.

To determine the significance of the SW temperature peak, we measured the projected temperature profile in four directions (see the angular sectors shown in Figure 6). Due to the limited number of counts, we chose only four bins per sector. We note that the amount of absorption can affect temperature measurements, with underestimated  $N_H$  biasing the temperature high. Since  $N_H$  is relatively large in this region of the sky, and may change across the field, the absorption was allowed to vary in each fit. The abundance was also allowed to vary. The resulting temperature profiles are shown in Figure 7. The highest temperature by far is to the SW, in the region of the temperature peak seen in the temperature map, with  $kT = 18.5 \pm 6.0$  keV. Compared with other sectors in the same radial range, this feature is significant at about  $1.8\sigma$  (see Section 5.1). Since  $N_H$  is allowed to vary, its uncertainty is folded into the temperature uncertainty. If we fix  $N_H$  at our best fitting global ICM value of  $3.5 \times 10^{21} \text{ cm}^{-2}$ , we find a statistically equivalent fit with  $kT = 14.6^{+2.4}_{-3.1}$  keV for the SW temperature peak. In this case, the temperature increase is significant at  $2.3\sigma$  as compared with other sectors in the same radial range also with  $N_H$  fixed at the global value. If we instead fix  $N_H$  at the LAB survey value of  $2.3 \times 10^{21} \text{ cm}^{-2}$  we find a somewhat worse statistical fit (with a null hypothesis probability of 2.8% versus 5.1% for the free  $N_H$  case) with  $kT = 30^{+9}_{-6}$  keV. For every annular bin, the best-fitting value of  $N_H$  is within  $2\sigma$  of the best-fitting global ICM value. Although the SW temperature peak is only marginally statistically significant, based on its location on the merger axis and correlation with the SW radio relic, as expected for a merger bow shock (see Section 5.1), we conclude that it is likely a real feature.

We note that, given the high temperature, lack of strong emission lines, and limited number of counts, we



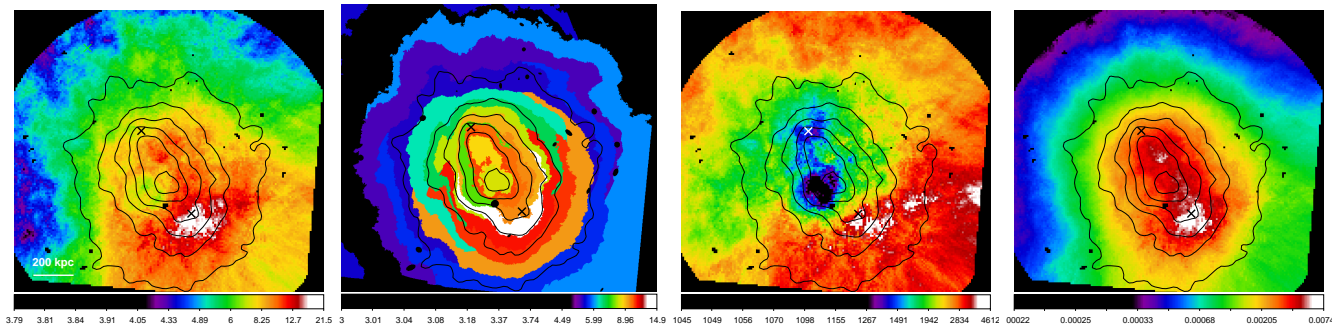


**Figure 5.** Left: Smoothed temperature map, in units of keV, with the *Chandra* surface brightness contours overlaid in black. Left-center: Contour binned temperature map of the same region. Right-center: Smoothed pseudo-entropy map, in arbitrary units, calculated as  $kTA^{-1/3}$ , where  $A$  is the APEC normalization scaled by the area of the extraction region (blue is low pseudo-entropy). The lowest entropy gas is extended from NE to SW, consistent with two partially disrupted, merging cluster cores. Right: Smoothed pseudo-pressure map, in arbitrary units, calculated as  $kTA^{1/2}$  (white is high pseudo-pressure). There is a pressure peak to the SW, coincident with the high temperature peak, consistent with the presence of a merger shock. The crosses mark the locations of the two BCGs in each panel.

cannot confirm the thermal nature of this emission (as compared with, e.g., inverse Compton emission from the interaction of the CMB with the radio emitting particles in this region, or emission from unresolved point sources associated with the nearby BCG). This issue is discussed further in Section 5.4.

#### 4. DIFFUSE RADIO EMISSION

The radio emission is shown in Figure 8, ranging from 74 MHz to 1.4 GHz. In van Weeren et al. (2011a), the diffuse 1.4 GHz radio emission was classified as a radio halo with a north-south extension, based on the continuous structure of the source and the rough correspondence with the low resolution *ROSAT* X-ray image. The new *Chandra* images reveal a NE-SW extension of the ICM, with a doubly peaked core (Section 3.2). In light of these new data, we suggest that the diffuse radio emission represents a two-sided radio relic, possibly with radio halo emission between the relics, as has been observed in other systems (e.g., Bagchi et al. 2006; van Weeren et al. 2011b, 2012a; de Gasperin et al. 2014), although other interpretations are possible. For a detailed discussion, see Section 5.3.1. For the purposes of this paper, we refer to the diffuse 1.4 GHz emission as a radio relic throughout.

The 1.4 GHz radio flux profile extracted from the box region shown in Figure 8 is compared with the X-ray surface brightness profile in the same region in Figure 4. The radio profile shows two clear peaks (in contrast with the single central peak expected for radio halos), which are at larger radii than the two bright X-ray peaks, in the regions of the BCGs and optical galaxy density peaks. The SW radio peak is roughly coincident with the SW temperature peak identified in Section 3.3. The observations are therefore consistent with what is expected for radio relics in a late stage merging system, where the relics trace ICM merger shocks, which lead the X-ray cores. The dynamical state of CIZA 0107 is discussed further in Section 5.1.

The 74 MHz image reveals an elongated structure, NW of the southern subcluster center, and a fainter secondary peak to the SE (Figure 8, lower right panel and blue contours). The NW feature is seen as an extended, possibly double peaked source at 150 MHz and 240 MHz, but is not visible at 610 MHz or 1.4 GHz (see the contours in Figure 8). It is not coincident with the brighter regions of the relic at 1.4 GHz, suggesting that it may be an unrelated feature. Similarly, the SE 74 MHz peak is seen

at 150 MHz, and possibly 240 MHz, but not at higher frequencies. Neither feature is clearly associated with a bright X-ray or optical source (see Figure 9).

In Table 1, we give radio fluxes at 1.4 GHz, 240 MHz, 150 MHz, and 74 MHz, along with some spectral indices, in three different regions: a larger region containing all of the diffuse emission detected at all frequencies, a smaller region corresponding to the NW USS source at 74 MHz, and a slightly smaller region corresponding to the SW USS source at 74 MHz. Fluxes were not calculated at 610 MHz since we expect some flux loss on the scale of the diffuse emission due to the lack of short baselines. To account for calibration uncertainties, we include a systematic error of 5% at 1.4 GHz, 10% at 240 MHz and 150 MHz, and 15% at 74 MHz. We follow the calibration uncertainties adopted by Lane et al. (2014) for the VLSSr data. For the WSRT and the GMRT, our adopted calibration uncertainties are based on our experience with working with data from these observatories, as we have done elsewhere (e.g., van Weeren et al. 2014). For the total emission in the region of the relic, we find spectral indices from 74 MHz to 150 MHz and 74 MHz to 240 MHz of  $\alpha_{74}^{150} = -1.2$  and  $\alpha_{74}^{240} = -1.4$ . For the NW, elongated structure detected at 74 MHz (Figure 8), we find significantly steeper emission, with  $\alpha_{74}^{150} = -2.3$  and  $\alpha_{74}^{240} = -2.1$ . Similarly, for the SE peak at 74 MHz we find  $\alpha_{74}^{150} = -2.2$  and  $\alpha_{74}^{240} = -2.1$  (see Figure 13). These features are discussed further in Section 5.3.2.

## 5. DISCUSSION

### 5.1. Cluster Dynamical State

X-ray and radio observations of CIZA 0107 show that it is a non-dynamically relaxed merger system, with the merger axis likely along the NE-SW direction. The overall X-ray emission is extended along this axis, with two X-ray surface brightness peaks along the same line, consistent with two merging subclusters. There is a high temperature region to the SW, along the merger axis, consistent with the presence of a merger bow shock leading the SW core. There is a hint of an excess in the X-ray surface brightness at this location (Figures 3 & 4), consistent with the presence of a shock, although this feature is only marginally significant. The radio emission is also extended from NE to SW, at multiple frequencies, with two bright peaks at 1.4 GHz roughly 200 kpc from the overall cluster center (the center of the annular bin

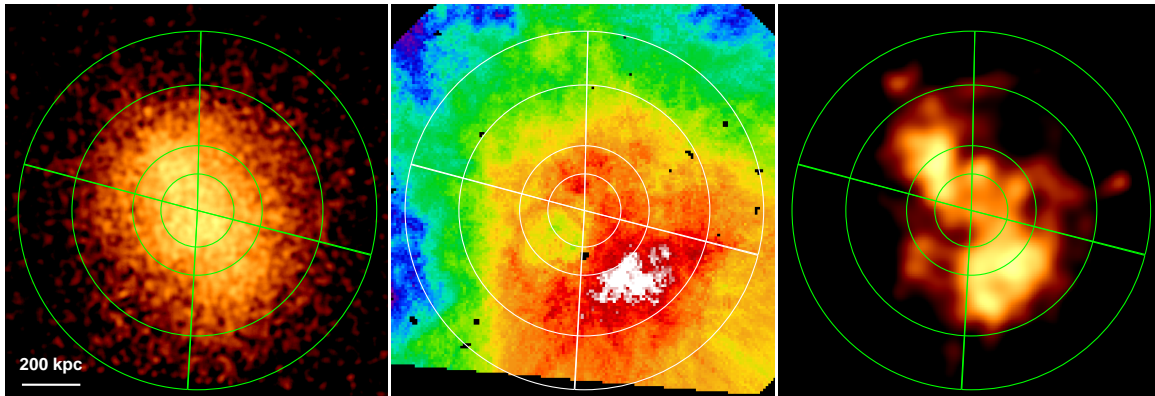


**Figure 6.** X-ray image (left), smoothed temperature map (center), and 1.4 GHz radio image (right) with the extraction regions used to make the profiles shown in Figure 7 overlaid.

**Table 1**  
Radio Source Properties

Source	$F_{1400}$ (mJy)	$F_{240}$ (mJy)	$F_{150}$ (mJy)	$F_{74}$ (mJy)	$\alpha_{74}^{240}$	$\alpha_{74}^{150}$
Total	$72 \pm 4.5$	$329 \pm 41$	$759 \pm 163$	$1779^a \pm 637$	$-1.4 \pm 0.3$	$-1.2 \pm 0.6$
NW USS Source	$29 \pm 1.9$	$174 \pm 21$	$420 \pm 80$	$2126 \pm 412$	$-2.1 \pm 0.2$	$-2.3 \pm 0.4$
SE USS Source	$6.8 \pm 0.9$	$66 \pm 10$	$159 \pm 50$	$778 \pm 223$	$-2.1 \pm 0.3$	$-2.2 \pm 0.6$

<sup>a</sup> We note that the 74 MHz flux in the total region is less than the sum of the fluxes in the NW and SE USS regions, which are contained within the total region. This is because the local noise level in the region of the cluster is biased negative due to imperfect calibration. The total and summed NW plus SE 74 MHz fluxes are consistent within  $1.5\sigma$ .

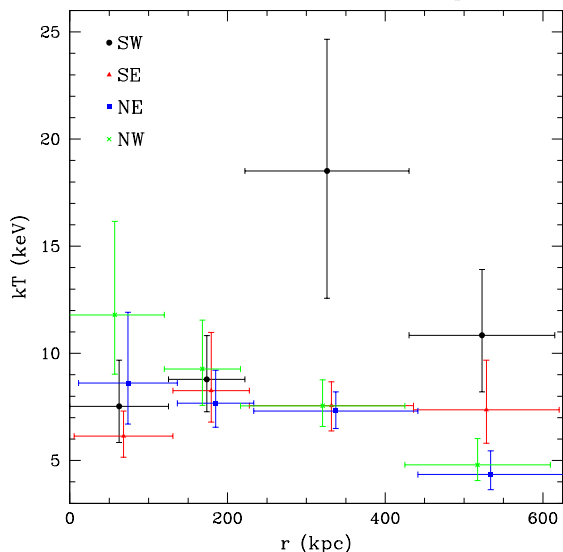


**Figure 7.** Temperature profile in the four sectors shown in Figure 6. Individual profiles have been shifted slightly in the radial direction for clarity.

regions shown in Figure 6). The SW radio peak is coincident with the SW shock region. This is consistent with a double radio relic, as seen in other merging systems, where particles in the ICM are (re)accelerated at the merger shock associated with each subcluster and emit synchrotron radiation.

The optical image is shown in Figure 10, with the *Chandra* X-ray surface brightness contours overlaid in red, and the optical flux-weighted cluster galaxy density contours overlaid in blue. This image shows two BCGs, indicated with green circles, consistent with two merging

subclusters. The SW BCG was identified by Crawford et al. (1995), with a reported redshift of  $z = 0.109$  (although this redshift is described as “provisional” due to poor S/N). Both of the optical galaxy density peaks and both BCGs lie on the merger axis, at larger radii than the X-ray peaks, and separated from one another by roughly 500 kpc in projection. We conclude that CIZA 0107 is likely a dissociative post-merger system, similar to the famous Bullet cluster (Markevitch et al. 2002; Markevitch & Vikhlinin 2007).

In this scenario, the diffuse ICM in the subcluster cores experiences ram pressure drag forces during the cluster merger, while the effectively collisionless galaxies and dark matter (DM) halos do not, leading to a separation between the ICM and galaxy/DM peaks. Therefore, the ICM is expected to trail the galaxies roughly along the merger axis (although the gas may lead the galaxies during the later stages of a merger due to the ram pressure slingshot effect, see Markevitch & Vikhlinin 2007). The ICM and galaxy density peak offsets indicate that this is a post core passage merging system. Thus we expect the NE X-ray and galaxy peaks to be moving NE, and their SW counterparts to the SW (in projection). As in the Bullet cluster, the SW galaxy density peak is at roughly the location of the SW leading bow shock. The lack of complicated structure in the ICM along with the subcluster cores, the merger shock, the radio relics, the optical galaxy density peaks, and the BCGs all lying roughly along the same line (i.e., the merger axis) suggest that this is a low impact parameter merger (at least in projection), also similar to the Bullet cluster.

Figure 7 shows a temperature increase between 200–400 kpc to the SW as compared with other sectors, which all have  $kT \approx 7.5$  keV. Averaging the NW, NE,

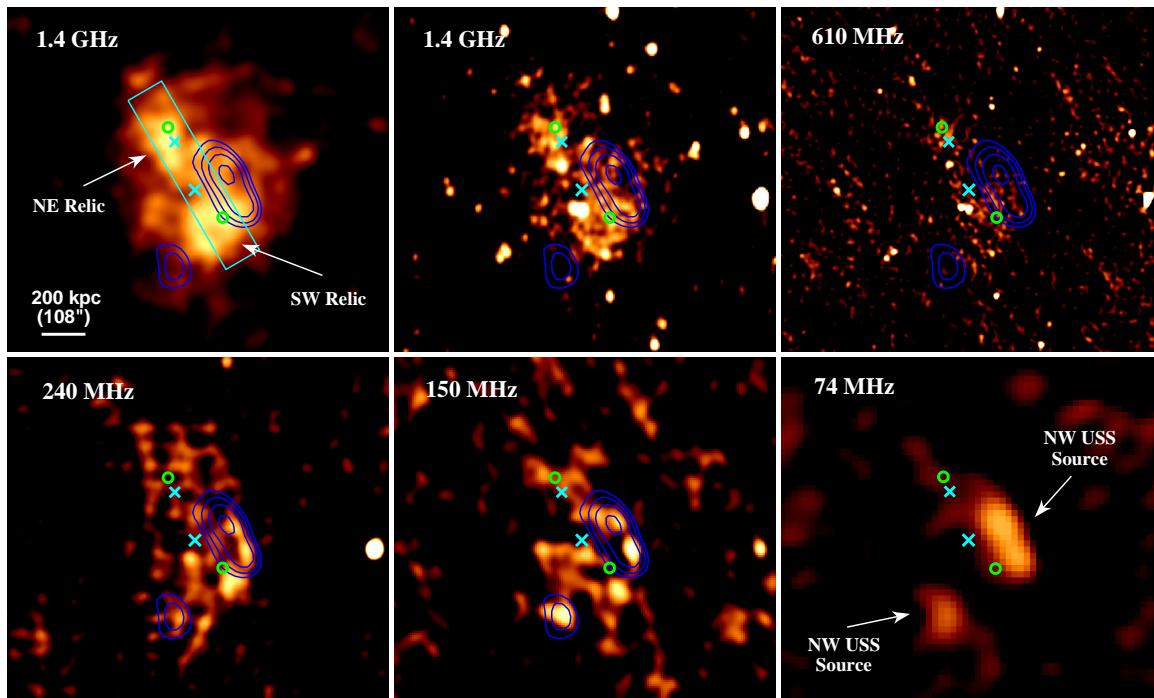


**Figure 8.** Top left: 1.4 GHz WSRT image (with a resolution of  $21'' \times 17''$  and a noise level of  $29 \mu\text{Jy beam}^{-1}$ ), with point sources removed, and smoothed with a  $40''$  radius Gaussian to highlight faint structure. The cyan box indicates the region used to extract the radio and X-ray profiles shown in Figure 4. Top-middle: 1.4 GHz WSRT image with point source included. Top right: 610 MHz GMRT image (with a resolution of  $5.7'' \times 4.1''$  and a noise level of  $54 \mu\text{Jy beam}^{-1}$ ), smoothed with a  $9''$  radius Gaussian. Bottom left: 240 MHz GMRT image (with a resolution of  $13.3'' \times 10.4''$  and a noise level of  $0.57 \text{ mJy beam}^{-1}$ ), smoothed with a  $24''$  radius Gaussian. Bottom center: 150 MHz GMRT image (with a resolution of  $29.5'' \times 21.9''$  and a noise level of  $13 \text{ mJy beam}^{-1}$ ), smoothed with a  $25''$  radius Gaussian. Bottom right: 73.8 MHz NRAO VLA VLSSr image (with a resolution of  $75''$  and a noise level of  $78 \text{ mJy beam}^{-1}$ ). The 73.8 MHz VLSS contours are shown in blue, they start at  $3\sigma$  ( $0.653 \text{ Jy beam}^{-1}$ ) and increase by factors of  $\sqrt{2}$ . The locations of the BCGs are indicated by green circles, and the locations of the two X-ray peaks shown in Figure 4 are indicated by cyan crosses. The double radio relic and USS sources have apparently uncorrelated morphologies. The relic is most clearly visible at 1.4 GHz, and is no longer detected at 74 MHz, while the USS sources are bright at 74 MHz, are somewhat visible up to 240 MHz, and are no longer detected at 1.4 GHz.

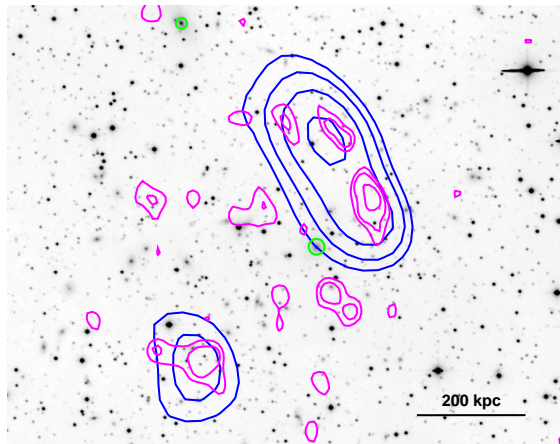


**Figure 9.** Optical INT *I* band image in the region for the USS radio sources. 74 MHz VLSSr contours are overlaid in blue, and 150 MHz GMRT contours are overlaid in magenta. Contours start at  $3\sigma$  at 74 MHz and  $1\sigma$  at 150 MHz and increase by factors of  $\sqrt{2}$ . The two BCGs are marked with green circles. There are no obvious optical point sources clearly associated with the USS diffuse radio sources.

and SE sectors together in this radial range, we find a temperature of  $kT = 7.5 \pm 0.6 \text{ keV}$ , as compared with  $kT = 18.5 \pm 6.0 \text{ keV}$  in the SW. Applying the standard Rankine-Hugoniot shock jump conditions for an ideal gas with a constant ratio of specific heats of  $\gamma = 5/3$ , this corresponds to a Mach number of  $M = 2.3 \pm 0.4$ . In prin-

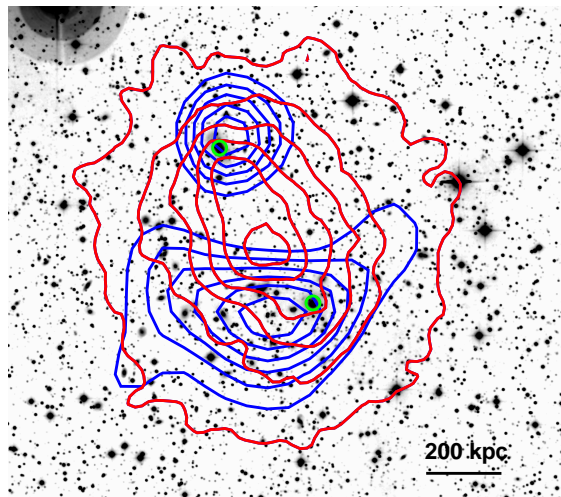


**Figure 10.** Optical INT *I* band image with *Chandra* X-ray contours overlaid in red; smoothed, source flux weighted galaxy number density contours overlaid in blue; and the locations of the BCGs indicated with green circles. The two optical galaxy density peaks are clearly offset from the peak of the X-ray emission along the merger axis, from NE to SW.

ciple, this is a lower limit on the true Mach number, since projection effects will tend to bias the measured temperature increase low. For a 7.5 keV gas, this Mach number corresponds to a relative ICM velocity of  $3250 \text{ km s}^{-1}$ . As shown by Springel & Farrar (2007), the Mach number

of an ICM merger shock can overestimate the relative velocity of the subcluster DM halos, as is likely the case for the Bullet cluster.

When viewed along a tangent line to the Mach cone, ICM shocks are expected to appear as sharp surface brightness edges in high angular resolution X-ray observations. However, no such edge is clearly visible in the region of the SW shock, neither in the X-ray image nor the unsharp-masked image. To further test for an edge in this region, we extracted the integrated emissivity profiles in the SW and NE sectors. These profiles were generated assuming the radial temperature profile in each sector followed the projected temperature profile (Figure 7) with the abundance fixed at  $Z = 0.3 Z_{\odot}$ . The results are shown fitted with a 3D  $\beta$ -model density profile in Figure 11. Both sectors are reasonably well-described by the model, with no clear evidence for an edge feature, although the SW profile shows weak evidence for a dip in the profile at  $\sim 370$  kpc, at the outer edge of the SW radio relic and high temperature region.

We modeled this dip using a discontinuous double power-law density profile of the form

$$n_e(r) = \begin{cases} n_0 \left(\frac{r}{r_{\text{br}}}\right)^{-k_1} & (r \leq r_{\text{br}}) \\ n_1 \left(\frac{r}{r_{\text{br}}}\right)^{-k_2} & (r > r_{\text{br}}) \end{cases}, \quad (1)$$

where  $r_{\text{br}}$  is the break radius. This model is shown fitted to the data in Figure 12. If we fix the break radius at  $r_{\text{br}} = 370$  kpc, we find evidence for a weak edge, corresponding to a density jump factor of  $1.2^{+0.1}_{-0.1}$ . However, if the location of the break radius is allowed to vary the profile is also well-fit by a model with no discontinuous jump and a change in slope at a smaller radius. The lack of an apparent sharp surface brightness edge may indicate that there is a line of sight component to this merger, such that the edge is diminished by projection effects, while the hot, shock-heated gas is still visible in projection, as has been reported for other systems, (e.g., A2443, Clarke et al. 2013; A2744, Owers et al. 2011). The angle between the merger axis and the plane of the sky needn't be very large to obfuscate shock edges (see Figure 18 in Owers et al. 2011). Additionally, it may be difficult to pick out edges by eye in this relatively shallow (23 ks) observation, especially in fainter regions where the image must be smoothed to show ICM structure. The radius of curvature of merger shock fronts is generally not expected to be centered on the cluster itself. Since we are unable to identify the location of the edge, we cannot match the radius of curvature, center, and bin boundary location of our profile extraction regions to the edge. This will effectively blur the edge in the extracted profile, making it more difficult to detect. We conclude that deeper observations are required to confirm or rule out the presence of a surface brightness edge in this region.

The BCG of each subcluster was observed with the Wide Field Grism Spectrograph 2 on the University of Hawaii 2.2-meter Mauna Kea telescope as part of the CIZA survey (Ebeling et al. 2002; Kocevski et al. 2007). They find redshifts of 0.103 for both of the BCGs (D. Kocevski private communication). While the exact uncertainty of these redshifts are not reported, they add to the supporting X-ray, radio, and optical imaging evidence that CIZA 0107 is composed of two nearby clusters

that are undergoing a major merger.

## 5.2. Dark Matter Self-Interaction Cross Section

Markevitch et al. (2004) outline four methods for placing constraints on the self-interaction cross-section of DM ( $\sigma_{\text{DM}}$ ) using dissociative mergers. Placing such constraints on  $\sigma_{\text{DM}}$  requires lensing observations to map the total mass distribution, as well as optical spectroscopy to identify subcluster member galaxies, optical centroids, and subcluster line-of-sight velocities, neither of which are currently available for CIZA 0107. Nevertheless, we can use simple estimates to show that this system can, in principle, provide competitive constraints on  $\sigma_{\text{DM}}$ . To this end, let us assume that the dark matter halos are centered on the optical galaxy density peaks shown in Figure 10. The offsets between the DM peaks and gas peaks indicates that the scattering depth of the DM particles cannot be much larger than 1, otherwise the DM subhaloes would experience drag forces similar to the gas and there would be no offset. Following Markevitch et al. (2004), we can write the subcluster DM scattering depth as

$$\tau_s = \frac{\sigma_{\text{DM}}}{m_{\text{DM}}} \Sigma_s, \quad (2)$$

where  $\Sigma_s$  is the DM surface mass density. To estimate  $\Sigma_s$ , we assume that the gas is isothermal and follows a single  $\beta$ -model density profile (which is roughly consistent with observations, see Figures 7 & 11), and that it is in hydrostatic equilibrium. The latter assumption is not strictly true for this merging system, but suffices for the simple estimate we make here. In this case, the total density profile can be written as

$$\rho(r) = \frac{3\beta kT}{4\pi G\mu m_p} \left[ \frac{x^2(3+x^2)}{(1+x^2)^2} \right], \quad (3)$$

where  $x \equiv r/r_c$ ,  $r_c$  and  $\beta$  are the core radius and index that describe the gas density profile,  $kT$  is the gas temperature, and  $\mu m_p$  is the average mass per gas particle. Integrating over a circular aperture with projected radius  $x_0$  and along the line of sight, and dividing by the area of the aperture, we find that the projected surface mass density is

$$\begin{aligned} \Sigma_s &= \frac{4}{x_0^2} \int_0^{x_0} x \int_x^\infty \frac{r\rho(r)}{\sqrt{r^2 - x^2}} dr dx \\ &= \frac{3\beta kT}{2G\mu m_p \sqrt{x_0^2 + r_c^2}}. \end{aligned} \quad (4)$$

From the IEM profile fits in Section 5.1, we find  $\beta \approx 1.8$  and  $r_c \approx 630$  kpc. For  $kT = 8$  keV, this gives  $\Sigma_s \approx 0.26 \text{ g cm}^{-2}$  within a fiducial projected radius of  $x_0 = 100$  kpc. From Equation 2 we then find that  $\sigma_{\text{DM}}/m_{\text{DM}} \lesssim 4 \text{ cm}^2 \text{ g}^{-1}$ . This can be compared with a similar estimate based on observations of the Bullet cluster, but with  $\Sigma_s$  measured from lensing observations rather than estimated based on scaling relations, which gives  $\sigma_{\text{DM}}/m_{\text{DM}} \lesssim 5 \text{ cm}^2 \text{ g}^{-1}$  (Markevitch et al. 2004).

We stress that, given the lack of gravitational lensing observations to locate the DM peaks, we do not consider our limit on  $\sigma_{\text{DM}}/m_{\text{DM}}$  to be meaningful (here, we have assumed that the DM peaks are coincident with the optical centroids, which would imply  $\sigma_{\text{DM}} = 0$ ). Rather,



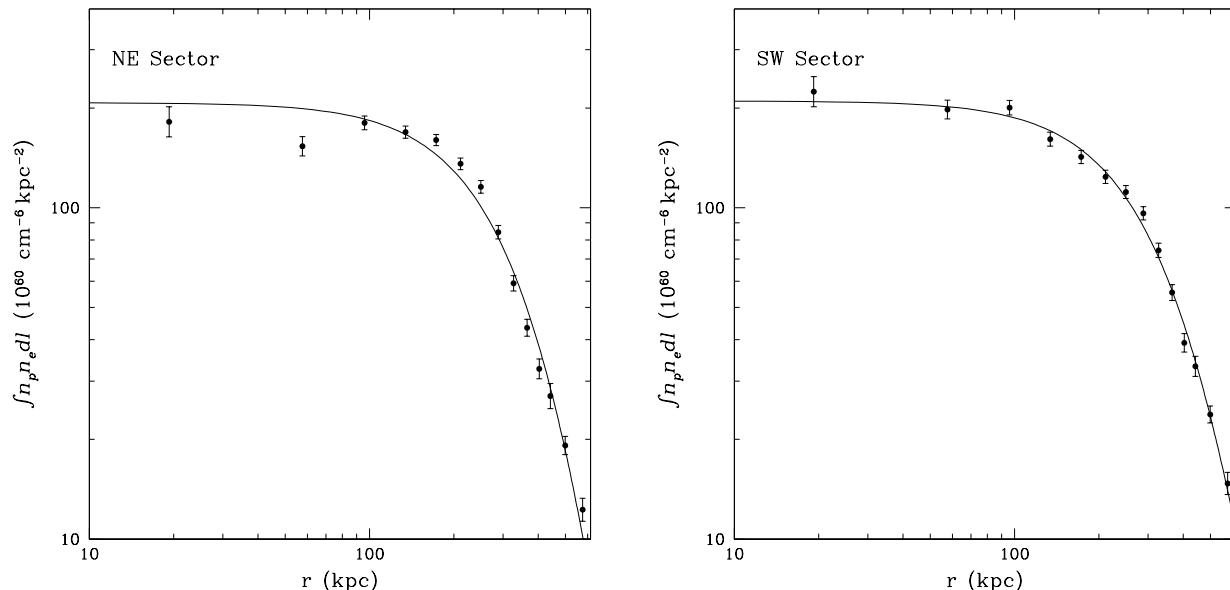


**Figure 11.** Integrated emissivity profiles in the SW and NE sectors. The solid lines show the best-fitting  $\beta$ -models.  $n_p$  and  $n_e$  are the proton and electron number densities, respectively, and the integral is taken along the line of sight  $l$ .

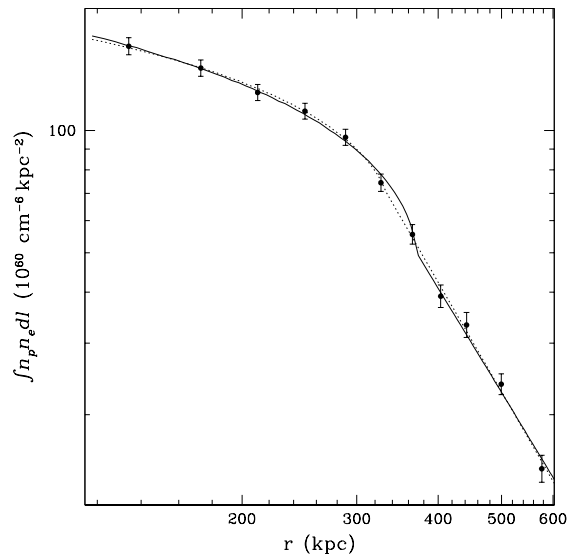


**Figure 12.** SW IEM profile fit with a discontinuous double power-law density profile with  $r_{\text{break}} \equiv 370$  kpc (solid line) and with a continuous double power-law model (dotted line).

the intent is to demonstrate that this system can potentially provide constraints on  $\sigma_{\text{DM}}/m_{\text{DM}}$  that are comparable to those derived for the Bullet cluster using similar methods, which currently provides the tightest constraints of any individual system known. Optical lensing and galaxy spectroscopy observations of CIZA 0107 will allow more accurate constraints to be placed on the DM self-interaction cross-section using a variety of methods, as has been done previously for the Bullet cluster (Markovitch et al. 2004; Randall et al. 2008b).

### 5.3. The Nature of the Diffuse Radio Emission

#### 5.3.1. High Frequency Diffuse Radio Emission

The radio image at 1.4 GHz shows two distinct peaks in the diffuse emission along the merger axis (Section 4, Figure 8). In principle, each peak may represent a radio relic associated with a merger shock, or a radio halo as-

sociated with a subcluster core. Double (as opposed to single) radio relics are not uncommon (e.g., van Weeren et al. 2011b; de Gasperin et al. 2014), while double radio halos are extremely rare but not undocumented (e.g., Murgia et al. 2010). There exists an empirical correlation between the radio halo power at 1.4 GHz,  $P_{1.4\text{GHz}}$ , and the 0.1–2.4 keV X-ray luminosity within  $r_{500}$ ,  $L_{X,500}$ . For the entire system, including both radio peaks, we find  $P_{1.4\text{GHz}} = 1.9 \times 10^{24} \text{ W Hz}^{-1}$  and  $L_{X,500} = 3.9 \times 10^{44} \text{ erg s}^{-1}$ . This places it somewhat above the  $P_{1.4\text{GHz}} - L_{X,500}$  relation of Cassano et al. (2013), although it is within the range of the scatter about this relation. Thus, we can not rule out a double radio halo interpretation of this based on the radio and X-ray powers. We note that we can likely exclude an AGN origin for this diffuse emission on Mpc scales since the synchrotron loss time is too short for electrons to have time to diffuse over these large regions (hence, in-situ particle acceleration is needed).

The SW radio peak is coincident with the high temperature, presumably shock-heated gas to the SW (Figures 5 & 7). It is offset from the SW X-ray peak by  $\sim 200$  kpc (Figure 4), roughly coincident with the SW BCG (Figure 8), inconsistent with what is expected for a radio halo, which should remain centered on the ICM of its host cluster. There is a hint of a small increase in X-ray surface brightness at the location of the SW radio peak (also seen as the faint peak to the SW in Figure 3), but this feature is too faint to be one of the main subcluster cores, and is instead likely due to ICM compression at the shock front. Given the coincidence with the high temperature region, a possible local increase in the X-ray surface brightness, its placement along the merger axis, and its separation from the X-ray surface brightness peak, we suggest that the SW radio peak may be a radio relic that has been energized by a local merger shock.

For the NE radio peak, the interpretation is less clear. The offset from the NE X-ray peak is smaller and less significant (Figure 4), and there is no indication of an

X-ray shock in this region. Thus, we conclude that this system is most likely either a double radio relic, possibly with a faint radio halo between the relics, or a SW radio relic and NE radio halo. Due to the relative rarity of these configurations, the double radio relic interpretation is probably more likely. The somewhat flocculent appearance of the relic, in contrast with the sharp, linear morphology of some other relics (e.g., van Weeren et al. 2012b), could in principle be due to a small inclination angle between the merger axis and the plane of the sky, as suggested by the lack of a sharp shock front edge in the X-ray (Section 5.1). For simplicity, we refer to the high frequency radio structure as a double radio relic, or simply “the relic”, throughout.

### 5.3.2. Ultra-Steep Spectrum Radio Sources

The 74 MHz radio image (Figure 8) shows two distinct peaks near the SW subcluster (an elongated structure to the NW, and a separate peak to the SE) that are not aligned with the merger axis, nor do they correlate with the brighter 1.4 GHz emission. The peaks become less prominent with increasing frequency, and are no longer visible at  $\nu \gtrsim 610$  MHz. This is a reflection of the very steep spectral indices of these sources, with  $\alpha_{\text{NE}} \approx \alpha_{\text{SW}} \approx -2$  (see Section 4). Neither source is clearly associated with a distinct radio, optical, or X-ray source (Figure 9).

The radio spectra in the regions of the two USS sources are shown in Figure 13, with lines of  $\alpha = -2.1$  normalized at 74 MHz overlaid. The spectra are consistent with power-laws at low frequency, but lie significantly above the extrapolated models at 1.4 GHz. This is consistent with the interpretation of the USS sources as unrelated to the radio relic, which is most clearly visible at 1.4 GHz, as suggested by the very different morphologies at 74 MHz and 1.4 GHz. Assuming a typical spectral index of  $\alpha = -1$  for the radio relic, we find that the observations are consistent with a non-detection at 74 MHz in the VLSSr.

Such diffuse, ultra-steep spectrum radio sources have been identified in other clusters (e.g., Slee et al. 2001; van Weeren et al. 2009; Randall et al. 2010; Ogrean et al. 2011; van Weeren et al. 2011c; Kale & Dwarakanath 2012; Clarke et al. 2013), but they are relatively rare, and the nature of these sources is not fully understood. Although we are unable to fit detailed models to the radio spectra of these sources since we only detect them at three frequencies, their steep spectra are consistent with old non-thermal electron populations that have been re-energized by a shock (i.e., radio phoenixes). According to this model, a pre-existing electron population (from, e.g., an old radio radio lobe) is re-energized by the passage of an ICM shock. Due to the high sound speed in the lobe, the plasma is not shocked, but rather compressed adiabatically (Enßlin & Gopal-Krishna 2001). This model can explain the lack of correlation between the low and high frequency radio emission, and the fact that the USS sources are displaced from the merger axis. The morphology of these sources depends on the spatial distribution of the pre-existing electron population, as opposed to classical radio relics which directly trace ICM shocks. The lack of obvious host galaxies for these sources is also consistent with this interpretation, since older radio lobes would have had time to detach from their hosts and fade

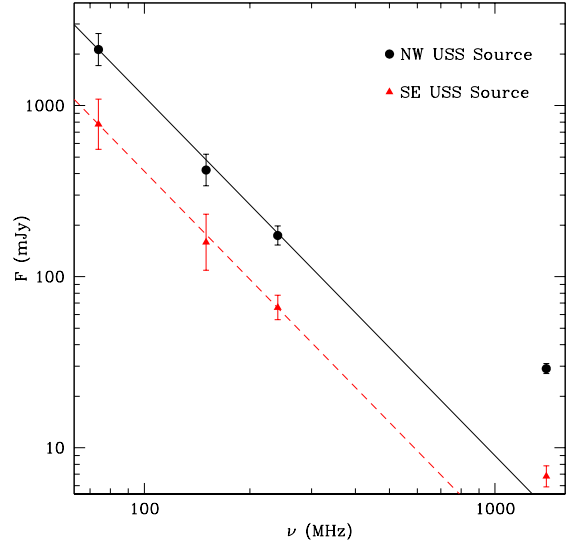


**Figure 13.** Radio spectral distribution in the region of the NW (black circles) and SE (red triangles) USS radio sources (which are most likely radio phoenixes). Power-laws with  $\alpha = -2.1$  (normalized at 74 MHz) are overlaid. The excess emission at 1.4 GHz is from the larger scale radio relic, and is likely unrelated to the radio phoenixes, as suggested by the uncorrelated morphologies (Figure 8).

before being re-energized by a merger shock.

### 5.3.3. Discussion

We conclude that the most likely interpretation of the observations is that the diffuse radio emission is from at least two distinct types of components: classical radio relics, where electrons are accelerated by a shock through, for example, diffusive shock acceleration (Drury 1983; Malkov & Drury 2001), and radio phoenixes, where old radio structures are re-energized by passing shocks through adiabatic compression. Both processes are driven by the same merger event. Thus, CIZA 0107 provides a relatively rare case of radio relics and radio phoenixes observed in the same system. USS sources have been identified as radio phoenixes in other merging systems (e.g., Clarke et al. 2013; de Gasperin et al. 2015), and therefore may provide a means of identifying dynamically disturbed systems from low frequency radio observations.

It is currently unclear whether relics and phoenixes represent different phases of a general “life-cycle” of non-thermal particles in the ICM, or whether they arise from distinct particle populations. I.e., radio lobes and phoenixes may eventually break apart, releasing their particles to the ICM and providing a diffuse non-thermal particle component that may be re-accelerated by ICM shocks to create radio relics. Alternatively, radio relic particles may have a different origin, e.g., they may be accelerated directly from the thermal pool. However, it seems unlikely that diffusive shock acceleration is efficient enough to accelerate particles from the thermal pool to the required energies (Enßlin et al. 1998; Pinzke et al. 2013). Furthermore, not all strong merger shocks are associated with radio relics (Russell et al. 2011), suggesting that the presence of a preexisting non-thermal particle population is required. High resolution, low frequency radio observations will help confirm the USS sources as radio phoenixes, which often have complicated, filamen-

tary morphologies (e.g., see Slee et al. 2001).

#### 5.4. Inverse Compton Emission

In principle, the high temperature peak to the SW seen in Figures 5 & 7 could arise from the contribution of a non-thermal component that is not included in our spectral model. In particular, we expect some level of inverse Compton (IC) emission due to the interaction of the synchrotron radio emitting electrons in the radio relic with the CMB. Despite this expectation, diffuse IC emission has yet to be conclusively detected in galaxy clusters (for recent results and reviews see Ota 2012; Wik et al. 2014; Gastaldello et al. 2015). To test for the presence of IC emission, we added a power-law component to the model for the high temperature bin roughly 330 kpc to the SW shown in Figure 7. We tried both allowing the temperature of the thermal component to vary and fixing it at the typical value at this radius of 8 keV. In neither case did including a power-law component significantly improve the fit.

To place a conservative limit on IC emission from this region, we fit the spectrum with an absorbed power-law, with no thermal component. This model provided a statistically equivalent fit to the single temperature thermal model, with an F-test probability of 72% (we consider an F-test probability of  $\lesssim 5\%$  to indicate a significant improvement). This degeneracy is due to our fairly shallow exposure, and to the lack of strong emission lines from such high temperature thermal plasma. The best-fit photon index was  $\Gamma = -1.5^{+0.1}_{-0.1}$ , which is close to the spectral slope of the radio emission  $\alpha_{74}^{240} = -1.3$  (Section 4). Assuming that the synchrotron and IC emitting particles are the same population, and that these particles follow a power-law distribution in energy, the synchrotron and IC spectral slopes are expected to be equal (Pacholczyk 1977). This model gives a total 2–10 keV flux of  $2.4^{+0.1}_{-0.1} \times 10^{-12}$  erg cm $^{-2}$  s $^{-1}$ .

Petrosian (2001) gives a convenient expression relating the monochromatic IC X-ray and synchrotron radio fluxes to the implied magnetic field strength,

$$R \equiv \frac{f_{\text{IC}}(kT)}{f_{\text{sync}}(\nu)} = 1.86 \times 10^{-8} \left( \frac{\text{photons}}{\text{cm}^2 \text{ s keV Jy}} \right) \times \left( \frac{kT}{20 \text{ keV}} \right)^{-\Gamma} \left( \frac{\nu}{\text{GHz}} \right)^{\Gamma-1} \times \left( \frac{T_{\text{CMB}}}{2.8 \text{ K}} \right)^{\Gamma+2} \left( \frac{B}{\mu\text{G}} \right)^{-\Gamma} c(p), \quad (5)$$

where  $\Gamma = (p+1)/2$ ,  $p$  is the power-law slope of the electron energy distribution  $N(E) \propto E^{-p}$ ,  $f_{\text{IC}}(kT)$  is the IC flux density at energy  $kT$ ,  $f_{\text{sync}}(\nu)$  is the synchrotron flux density at frequency  $\nu$ ,  $T_{\text{CMB}}$  is the CMB temperature at the cluster redshift, and  $c(p)$  is a normalization factor that is a complicated function of  $p$  (with values  $10 < c(p) < 1000$  for typical values of  $p$ , see Rybicki & Lightman 1979). For  $2 \lesssim p \lesssim 5$ ,  $c(p)$  can be approximated as  $c(p) \approx e^{1.42p-0.51}$ . Using this approximation with Equation 5 and solving for the magnetic field, one

finds

$$B = \left( \frac{20 \text{ keV}}{kT} \right) \left( \frac{\nu}{\text{GHz}} \right)^{(p-1)/(p+1)} e^{\frac{2.84(p-r)}{p+1}} \mu\text{G}, \quad (6)$$

$$r = 0.7 \ln \left[ \frac{R_{\text{obs}}(kT, \nu)}{1.11 \times 10^{-8}} \right].$$

Note that there is a typo in the exponential term in the equivalent expression in Petrosian (2001) (their Equation 7). Our power-law fits in this region give an IC flux density of  $F_{\text{IC}}(1 \text{ keV}) = 4.8 \times 10^{-4}$  photons cm $^{-2}$  s $^{-1}$  keV $^{-1}$ , while the radio observations give  $F_{\text{sync}}(1.4 \text{ GHz}) = 1.35 \times 10^{-2}$  Jy (for the latter, bright point sources have been removed to give the flux of the diffuse emission only). For  $\Gamma = 1.55$ , this gives a magnetic field strength of  $B = 0.01 \mu\text{G}$ .

Since the X-ray surface brightness does not correlate with the radio emission in detail, and since diffuse IC flux has yet to be conclusively detected in deep observations of other galaxy clusters, we conclude that the thermal model is much more likely, despite the fact that the thermal and non-thermal models provide statistically equivalent fits. Since the non-thermal model assumes that all of the emission in this region is IC emission, whereas it is in fact very likely dominated by thermal ICM emission, the above flux is a very conservative upper limit on the true IC flux, and thus  $B > 0.01 \mu\text{G}$  is a very conservative lower limit on the magnetic field strength. For comparison, the equipartition magnetic field strength implied by the total diffuse 1.4 GHz flux is roughly  $1.6 \mu\text{G}$ , assuming a ratio of energy in protons to energy in electrons of  $k = 1$  and a minimum Lorentz factor of  $\gamma_{\text{min}} = 100$ .

## 6. SUMMARY

We present results from X-ray, optical and radio observations of the massive galaxy cluster CIZA J0107.7+5408. Observations at all three wavelengths show a double-peaked morphology, with all peaks lying along roughly the same axis. The optical and 1.4 GHz radio peaks are at larger cluster radii than the X-ray peaks. The X-ray temperature map reveals a high temperature peak to the SW, roughly coincident with the SW radio peak at 1.4 GHz. We conclude that this system is a post core passage dissociative merger. The X-ray peaks lag the optical galaxy density peaks due to ram pressure forces on the ICM. Merger shocks lead the merging subclusters, giving rise to the possible doubly peaked radio relic and the shock heated gas in the region of the SW relic. The SW temperature rise implies a shock Mach number of at least  $M = 2.3 \pm 0.4$ . Rough estimates suggest that follow up optical lensing and spectroscopic observations may allow interesting limits to be placed on the self-interaction cross-section of dark matter, as has been done for other dissociative merging systems.

Low frequency radio observations reveal diffuse, ultra-steep spectrum radio emission, with  $\alpha \approx -2$ . This emission shows two peaks near the SW subcluster, although the peaks do not correlate with the merger axis, the X-ray emission, or the high frequency radio emission (i.e., the radio relics). We suggest that these features are radio phoenixes, formed when old but relatively cohesive radio structures (likely created by radio galaxies) are re-energized due to adiabatic compression by passing

merger shocks. Thus, CIZA 0107 is a relatively rare case containing clear examples of both classical radio relics and USS radio phoenixes.

Finally, we use the X-ray observations to place very conservative upper limits on the IC flux, and lower limits on the ICM magnetic field strength, in the region of the SW relic.

#### ACKNOWLEDGMENTS

Support for this work was partially provided by the Chandra X-ray Center through NASA contract NAS8-03060, the Smithsonian Institution, and by the *Chandra* X-ray Observatory grant GO3-14134X. Basic research in radio astronomy at the Naval Research Laboratory is supported by 6.1 Base funding. This research has made use of the NASA/IPAC Extragalactic Database (NED), which is operated by the Jet Propulsion Laboratory, California Institute of Technology, under contract with the National Aeronautics and Space Administration. We thank the staff of the GMRT who have made these GMRT observations possible. GMRT is run by the National Centre for Radio Astrophysics of the Tata Institute of Fundamental Research. The National Radio Astronomy Observatory is a facility of the National Science Foundation operated under cooperative agreement by Associated Universities, Inc. We thank Dale Kocevski for providing spectroscopic redshifts for the BCGs, and Paul Nulsen for useful discussions.

#### REFERENCES

- Bagchi, J., Durret, F., Neto, G. B. L., & Paul, S. 2006, *Science*, 314, 791
- Bertin, E., & Arnouts, S. 1996, *A&AS*, 117, 393
- Blandford, R., & Eichler, D. 1987, *Phys. Rep.*, 154, 1
- Bradač, M., Clowe, D., Gonzalez, A. H., et al. 2006, *ApJ*, 652, 937
- Brunetti, G., & Jones, T. W. 2015, in *Astrophysics and Space Science Library*, Vol. 407, *Magnetic Fields in Diffuse Media*, ed. A. Lazarian, E. M. de Gouveia Dal Pino, & C. Melioli, 557
- Brunetti, G., Setti, G., Feretti, L., & Giovannini, G. 2001, *MNRAS*, 320, 365
- Cassano, R., Ettori, S., Brunetti, G., et al. 2013, *ApJ*, 777, 141
- Clarke, T. E., Randall, S. W., Sarazin, C. L., Blanton, E. L., & Giacintucci, S. 2013, *ApJ*, 772, 84
- Clowe, D., Bradač, M., Gonzalez, A. H., et al. 2006, *ApJ*, 648, L109
- Clowe, D., Randall, S. W., & Markevitch, M. 2007, *Nuclear Physics B Proceedings Supplements*, 173, 28
- Crawford, C. S., Edge, A. C., Fabian, A. C., et al. 1995, *MNRAS*, 274, 75
- Dawson, W. A., Wittman, D., Jee, M. J., et al. 2012, *ApJ*, 747, L42
- de Gasperin, F., Ogrean, G. A., van Weeren, R. J., et al. 2015, *MNRAS*, 448, 2197
- de Gasperin, F., van Weeren, R. J., Brüggen, M., et al. 2014, *MNRAS*, 444, 3130
- Drury, L. O. 1983, *Reports on Progress in Physics*, 46, 973
- Ebeling, H., Mullis, C. R., & Tully, R. B. 2002, *ApJ*, 580, 774
- Ensslin, T. A., Biermann, P. L., Klein, U., & Kohle, S. 1998, *A&A*, 332, 395
- Enßlin, T. A., & Gopal-Krishna. 2001, *A&A*, 366, 26
- Fabian, A. C., Sanders, J. S., Taylor, G. B., et al. 2006, *MNRAS*, 366, 417
- Feretti, L., Giovannini, G., Govoni, F., & Murgia, M. 2012, *A&A Rev.*, 20, 54
- Foster, A. R., Ji, L., Smith, R. K., & Brickhouse, N. S. 2012, *ApJ*, 756, 128
- Gastaldello, F., Wik, D. R., Molendi, S., et al. 2015, *ApJ*, 800, 139
- Grevesse, N., & Sauval, A. J. 1998, *Space Sci. Rev.*, 85, 161
- Harvey, D., Massey, R., Kitching, T., Taylor, A., & Tittley, E. 2015, *Science*, 347, 1462
- Intema, H. T. 2014, *ArXiv e-prints*, arXiv:1402.4889
- Intema, H. T., van der Tol, S., Cotton, W. D., et al. 2009, *A&A*, 501, 1185
- Kalberla, P. M. W., Burton, W. B., Hartmann, D., et al. 2005, *A&A*, 440, 775
- Kale, R., & Dwarakanath, K. S. 2012, *ApJ*, 744, 46
- Kocevski, D. D., Ebeling, H., Mullis, C. R., & Tully, R. B. 2007, *ApJ*, 662, 224
- Lane, W. M., Cotton, W. D., van Velzen, S., et al. 2014, *MNRAS*, 440, 327
- Malkov, M. A., & Drury, L. O. 2001, *Reports on Progress in Physics*, 64, 429
- Markevitch, M., Gonzalez, A. H., Clowe, D., et al. 2004, *ApJ*, 606, 819
- Markevitch, M., Gonzalez, A. H., David, L., et al. 2002, *ApJ*, 567, L27
- Markevitch, M., & Vikhlinin, A. 2007, *Phys. Rep.*, 443, 1
- Murgia, M., Govoni, F., Feretti, L., & Giovannini, G. 2010, *A&A*, 509, A86
- Murgia, M., Markevitch, M., Govoni, F., et al. 2012, *A&A*, 548, A75
- Ogrean, G. A., Brüggen, M., van Weeren, R., et al. 2011, *MNRAS*, 414, 1175
- Ota, N. 2012, *Research in Astronomy and Astrophysics*, 12, 973
- Owers, M. S., Randall, S. W., Nulsen, P. E. J., et al. 2011, *ApJ*, 728, 27
- Pacholczyk, A. G. 1977, *Oxford Pergamon Press International Series on Natural Philosophy*, 89
- Peek, J. E. G., Heiles, C., Douglas, K. A., et al. 2011, *ApJS*, 194, 20
- Petrosian, V. 2001, *ApJ*, 557, 560
- Pinzke, A., Oh, S. P., & Pfrommer, C. 2013, *MNRAS*, 435, 1061
- Planck Collaboration, Ade, P. A. R., Aghanim, N., et al. 2014, *A&A*, 571, A29
- Randall, S., Nulsen, P., Forman, W. R., et al. 2008a, *ApJ*, 688, 208
- Randall, S. W., Clarke, T. E., Nulsen, P. E. J., et al. 2010, *ApJ*, 722, 825
- Randall, S. W., Markevitch, M., Clowe, D., Gonzalez, A. H., & Bradač, M. 2008b, *ApJ*, 679, 1173
- Randall, S. W., Sarazin, C. L., & Ricker, P. M. 2002, *ApJ*, 577, 579
- Ricker, P. M., & Sarazin, C. L. 2001, *ApJ*, 561, 621
- Röttgering, H., Afonso, J., Barthel, P., et al. 2011, *Journal of Astrophysics and Astronomy*, 32, 557
- Russell, H. R., van Weeren, R. J., Edge, A. C., et al. 2011, *MNRAS*, 417, L1
- Rybicki, G. B., & Lightman, A. P. 1979, *Radiative processes in astrophysics*
- Sanders, J. S. 2006, *MNRAS*, 371, 829
- Scaife, A. M. M., & Heald, G. H. 2012, *MNRAS*, 423, L30
- Slee, O. B., Roy, A. L., Murgia, M., Andernach, H., & Ehle, M. 2001, *AJ*, 122, 1172
- Springel, V., & Farrar, G. R. 2007, *MNRAS*, 380, 911
- Swarup, G. 1991, in *Astronomical Society of the Pacific Conference Series*, Vol. 19, *IAU Colloq. 131: Radio Interferometry. Theory, Techniques, and Applications*, ed. T. J. Cornwell & R. A. Perley, 376–380
- van Haarlem, M. P., Wise, M. W., Gunst, A. W., et al. 2013, *A&A*, 556, A2
- van Weeren, R. J., Bonafede, A., Ebeling, H., et al. 2012a, *MNRAS*, 425, L36
- van Weeren, R. J., Brüggen, M., Röttgering, H. J. A., et al. 2011a, *A&A*, 533, A35
- van Weeren, R. J., Hoeft, M., Röttgering, H. J. A., et al. 2011b, *A&A*, 528, A38
- van Weeren, R. J., Röttgering, H. J. A., & Brüggen, M. 2011c, *A&A*, 527, A114
- van Weeren, R. J., Röttgering, H. J. A., Brüggen, M., & Cohen, A. 2009, *A&A*, 508, 75
- van Weeren, R. J., Röttgering, H. J. A., Intema, H. T., et al. 2012b, *A&A*, 546, A124
- van Weeren, R. J., Intema, H. T., Lal, D. V., et al. 2014, *ApJ*, 781, L32
- Vikhlinin, A., Burenin, R. A., Ebeling, H., et al. 2009, *ApJ*, 692, 1033
- Wik, D. R., Hornstrup, A., Molendi, S., et al. 2014, *ApJ*, 792, 48